

Emergence of half-metallic ferromagnetism and valley polarization in transition metal substituted WSTe monolayer

Shivani Kumawat,¹ Chandan Kumar Vishwakarma,² Mohd Zeeshan,¹ Indranil Mal,¹ Sunil Kumar,^{1,*} and B. K. Mani^{1,†}

¹*Department of Physics, Indian Institute of Technology, Hauz Khas, New Delhi 110016, India*

²*Materials Department, University of California, Santa Barbara, California 93106-5050, USA*

(Dated: December 17, 2024)

Two-dimensional (2D) Janus materials hold a great importance in spintronic and valleytronic applications due to their unique lattice structures and emergent properties. They intrinsically exhibit both an in-plane inversion and out-of-plane mirror symmetry breakings, which offer a new degree of freedom to electrons in the material. One of the main limitations in the multifunctional applications of these materials is, however, that, they are usually non-magnetic in nature. Here, using first-principles calculations, we propose to induce magnetic degree of freedom in non-magnetic WSTe via doping with transition metal (TM) elements – Fe, Mn and Co. Further, we comprehensively probe the electronic, spintronic and valleytronic properties in these systems. Our simulations predict intrinsic Rashba and Zeeman-type spin splittings in pristine WSTe. The obtained Rashba parameter is ~ 422 meVÅ along the $\Gamma - K$ direction. Our study shows a strong dependence on uniaxial and biaxial strains where we observe an enhancement of $\sim 2.1\%$ with 3% biaxial compressive strain. The electronic structure of TM-substituted WSTe reveals half-metallic nature for 6.25 and 18.75% of Fe, 25% of Mn, and 18.75 and 25% of Co structures, which leads to 100% spin polarization. The structural asymmetry, strong SOC, and broken inversion symmetry are found to lead to valley polarization in TM-WSTe systems. The obtained values of valley polarization 65, 54.4 and 46.3 meV for 6.25% of Fe, Mn and Co, respectively, are consistent with the literature data for other Janus materials. Further, our calculations show a strain dependent tunability of valley polarization, where we find an increasing (decreasing) trend with uniaxial and biaxial tensile (compressive) strains. We observed a maximum enhancement of $\sim 1.72\%$ for 6.25% of Fe on application of 3% biaxial tensile strain. The ability to control valley degrees of freedom, along with spin and charge, could open a new prospect for next-generation spintronic and valleytronic devices.

I. INTRODUCTION

Analogous to the charge in electronics, spin degree of freedom (SDF) plays a crucial role in the field of spintronics [1]. Owing to their much faster speed, ultra-low heat dissipation and non-volatility, spintronic devices are more suitable in comparison to their electronic counterparts [2]. One of the key features of a spintronic material is the spin polarization, which is attributed to the differences in the population of spin-up and spin-down electrons. 2D materials have been demonstrated show significant advantages for spintronic applications [3, 4]. One of the primary benefits with 2D materials is their ability to exhibit intrinsic magnetism and half-metallicity at nanoscale. Experimentally, the room temperature ferromagnetism has been observed in transition metals doped 2D materials – Fe-doped MoS₂ [5], V-doped WSe₂ [6], V-doped MoTe₂ [7], Fe-doped ZrS₂ [8], TM (V, Cr, Mn, Fe, Co, Ni, and Cu)-doped black phosphorus [9].

In recent years, a new quantum degree of freedom, the valley degree of freedom (VDF), has emerged as a promising basis for device applications [10–13]. The energy levels of electrons in valence and conduction bands of a 2D material exhibit multiply degenerate extrema, known as valleys [14, 15]. The VDF based functional properties provide a roadmap for investigating the phenomena like optical circular dichroism, valley Hall effect and spin-valley locking [16–18] in the materials. One of key prerequisites in the practical realization of

VDF based applications is, however, the precise production and control of valley polarization. The valley polarization can be induced in 2D materials by lifting the energy degeneracy at K and K' valleys, and for this magnetic doping is suggested to be one of the efficient mechanisms [19]. In terms of experiments, the first demonstration of valley related physics in a 2D material was presented in the case of graphene [11]. Another key experiment, Ref. [12, 20], demonstrated inducing and controlling valley polarization in MoS₂ monolayer using circularly polarized light. Further, in a recent experiment, Sahoo *et al.* reported a high degree of valley polarization at room-temperature in Vanadium-doped MoS₂ [21]. In terms of simulations, Refs. [22] (MoSSe) and [23] (WSSe) have shown that the valley polarization can be induced in Janus 2D materials via transition metal dopings. Considering the previous experimental and theoretical studies in literature, it can thus be surmised that the TM-doping in non-magnetic 2D materials could provide a mechanism to induce spintronics and valleytronics properties.

The present work aims to explore and propose a material which could offer both spintronics and valleytronic properties. For this, we have identified a new class of 2D materials, Janus-transition-metal-dichalcogenides (Janus-TMDCs), WSTe, and its doping with transition metal elements. The reason for choosing this material for our study is, a research gap in terms of the understanding the effect of TM-doping on the properties of WSTe. It is to be mentioned that, its parent compound WTe₂ is reported to show a giant valley polarization, which is large enough to realize anomalous valley Hall effect, when doped with Co [24]. It should be noted that, due to their unique lattice structure and the absence of out-of-plane mir-

* kumarsunil@physics.iitd.ac.in

† bkmami@physics.iitd.ac.in

ror symmetry, Janus-TMDCs and based heterostructures have gained a tremendous attention for spintronic and valleytronics applications [25–27].

More precisely, in this work, with the help of the state-of-the-art first-principles calculations, we aim to probe electronic, spintronic and valleytronic properties in transition metals (Fe, Mn and Co)-substituted Janus WSTe monolayer. To probe it in a comprehensive way, we aim to address the following properties: i) The nature of electronic structure of pristine and TM-substituted WSTe (TM-WSTe) monolayer. ii) Rashba and Zeeman spin splittings in WSTe and their tunability using strain. iii) The impact of TM-substitution in terms of induced magnetic properties in WSTe. iv) Mechanism behind the advent of magnetic degrees of freedom in TM-WSTe and spin polarization. v) Probing the valley polarization and its tunability using uniaxial and biaxial strains.

The paper is organized into four sections. In Sec. II, we provide a brief description of the computational methods and parameters used in our calculations. In Sec. III, we present and analyze our results on electronic structure, magnetic properties, Rashba and Zeeman spin splittings, and valley polarization in TM-substituted WSTe. The summary of our results is presented in the last section of the paper.

II. COMPUTATIONAL METHODOLOGY

To investigate the properties of WSTe and TM-WSTe from first-principles, we performed the density functional theory (DFT) based calculations using *Vienna Ab initio Simulation Package* (VASP) package [28–30]. We used generalized gradient approximation (GGA) based Perdew-Burke-Ernzerhof (PBE) pseudopotential [31] to incorporate the exchange-correlations among electrons. The plane wave basis with an energy cutoff of 500 eV and the projector augmented wave [32] to represent atomic cores were employed in all the calculations. For all self-consistent-field calculations we used energy and force convergence criteria of 10^{-6} eV and 10^{-4} eV/Å, respectively. The Γ -centered k -mesh of $13 \times 13 \times 1$ was used in all calculations. The computed properties were, however, tested for convergence using higher k -mesh values. The effect of strongly correlated d -electrons of Fe/Mn/Co in TM-WSTe was incorporated using the rotationally invariant DFT+U approach of Dudarev *et al.* [33]. The Hubbard U parameters were calculated self-consistently using density functional perturbation theory (DFPT) employing the cococcioni’s approach [34]. Our computed values 4.4, 4.6, and 5.3 eV for Fe, Mn, and Co, respectively, are consistent with the values 4.6, 4.0, and 5.0 eV reported in the literature [35]. The small difference could be attributed to the difference in the pseudopotentials used and methods employed in the two calculations.

Further, to probe the Rashba and Zeeman-spin splittings, and valley polarization, we incorporated the relativistic effects using spin-orbit coupling (SOC) in our calculations. To avoid any artificial interaction between layers, a 12 Å thick vacuum was introduced along the z -direction in WSTe and TM-WSTe structures. To incorporate the substitution of transition met-

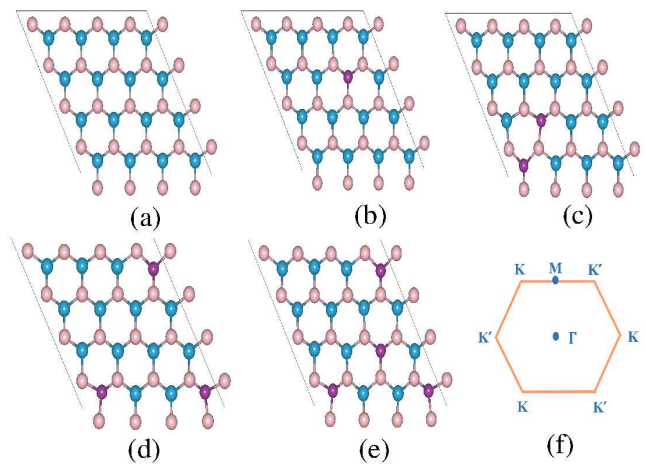


FIG. 1. Top view of (a) crystal structure of pristine WSTe. panels (b), (c), (d), and (e) show the crystal structure of Fe-WSTe for 6.25, 12.5, 18.75, and 25% concentrations. Blue, pink and purple spheres represent W, S, and Fe atoms, respectively. (f) 2D Brillouin zone of WSTe monolayer showing equivalent high-symmetry points.

als at W site, a $4 \times 4 \times 1$ supercell of WSTe monolayer was used. Considering the data available in literature and increasing computational complexity with smaller concentrations, we chose TM concentrations as 6.25, 12.50, 18.75, and 25% in our study.

III. RESULTS AND DISCUSSION

A. Crystal Structure and Structural Stability

The Janus TMDs, represented as MX_2 (where $M = \text{Mo}$ or W and $X, Y = \text{S}, \text{Se}, \text{or Te}$), exhibit a similar crystal structure as their parent material MX_2 , in which metal atoms are placed between the two layers of chalcogen atoms and form a hexagonal lattice. Therefore, the Janus monolayer structure originates from that of the TMDs with one layer of chalcogen atoms replaced with another group-VI elements. Bulk TMDs exist in 2H phase with space group $D6h$ which possesses inversion symmetry. However, for a monolayer, the crystal symmetry is reduced to $D3h$ for MX_2 and $C3v$ for MX_2 , and the inversion symmetry is violated. The crystal structure of pristine WSTe Janus monolayer is shown in the panel (a) of the Fig. 1.

We begin by optimizing the crystal structure of WSTe to achieve the global minimum ground state. For this, as there are no experimental inputs available for WSTe, we start with the experimental structure of WS_2 [36] and perform full relaxation calculations after replacing one S atom with Te atom. The optimized structural parameters from our calculations are provided in Table I. Our computed lattice parameters for pristine WSTe are in good agreement with the previous calculations [37, 38]. From our calculations we find that, there is no significant change in the lattice parameters after the TM-substitutions. This is consistent with the previous theory cal-

calculation for TM-substituted WSSe [23]. Table I also displays the bond lengths and bond angles for TM-WSTe, where L_1 and L_2 represent the bond lengths between W and S, and W and Te atoms, respectively. And θ is the angle between W and the surrounding S and Te atoms. As evident, both L_1 and L_2 decrease after the substitution of TM-elements, suggesting a stronger covalent interaction between the dopants and WSTe. A similar trend is also reported in TM substituted MoSeTe [39]. Since pristine WSTe has a graphene-like honeycomb structure, there are a series of equivalent high-symmetry K points in the Brillouin zone, which are shown in panel (f) of Fig. 1 for the use in the later part of the paper for discussion. The panels (b), (c), (d), and (e) show the crystal structure of Fe-WSTe for 6.25, 12.5, 18.75, and 25% concentrations.

Further, to check the stability of TM-WSTe structures, we examined the binding energy for all the considered concentrations. The data from this are given Table I. The observed negative values of binding energy confirm the relative stability of TM-WSTe structures.

B. Electronic Structure and Rashba Spin Splitting

Fig. 2 shows the electronic band structure for pristine WSTe without and with spin-orbit coupling. As discernible from the panel (a) of the figure, WSTe is an indirect band gap semiconductor, with a computed band gap of 1.35 eV. The valence band maximum (VBM) lies at the Γ point, whereas the conduction band minimum (CBM) lies between the Γ and K points. However, when the spin-orbit coupling is switched on, the band gap decreases to 1.21 eV. Moreover, we observed distinct spin splittings at K and K' valleys (panel (b)). We observed Rashba splitting at Γ point, which will be discussed in detail in subsequent sections. The valence and conduction bands edges are observed to be dominated by 5d-orbitals of W, 3p-orbitals of S and 5p-orbitals of Te atoms. The predicted electronic structure from our calculations for WSTe is in good agreement with the previous calculations [37, 38]. To get further insight into the electronic structure, we examined the atom and orbital-projected density of states (pDOS) of WSTe. The data from this are shown in the panels (c) and (d) of the figure. The spin-up and spin-down states are observed to be symmetric, implying the non-magnetic nature of the pristine WSTe. Looking into the orbital project DOS, we find that, consistent with the band structure, for both valence and conduction bands, the dominant contribution comes from the d -electrons of W atoms. The next significant contribution is observed from the p -electrons of S and Te atoms.

In WSTe monolayer, the combination of time-reversal and broken inversion symmetries along with a strong spin-orbit coupling is reported to break the spin degeneracy in the valence and conduction bands. This can result into two types of spin splittings – the Zeeman and Rashba spin splittings. The Zeeman-type spin splitting occurs essentially due to the strong spin-orbit coupling arising from W atom and the absence of inversion symmetry [40]. The Rashba-type spin splitting is, however, associated with the presence of an internal electric field perpendicular to the plane of the material [40]. In the

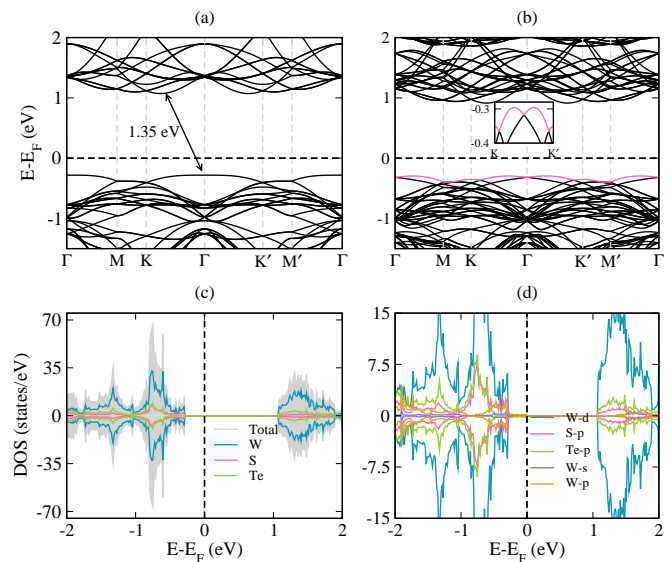


FIG. 2. The electronic band structure of WSTe, (a) without and (b) with spin-orbit coupling. The inset in panel (b) shows the Rashba splitting at the Γ point of VBM. Panel (c) and (d) show the atom and orbital-projected density of states, respectively. The Fermi level is set to zero.

present case of WSTe, this internal electric is developed due to the difference in electronegativities of S and Te atoms. For a 2D material, the Rashba spin splitting can be explained using the Hamiltonian [41]

$$H_R = \alpha_R (\hat{e}_z \times \vec{k}_{\parallel}) \cdot \vec{\sigma}, \quad (1)$$

where α_R is referred to as the Rashba parameter and signifies the strength of the effect. And, \hat{e}_z , \vec{k}_{\parallel} , and $\vec{\sigma}$ represent the unit vector along field direction, momentum of electron, and the Pauli spin matrices, respectively.

Fig. 3 shows the zoomed view of electronic band structure of WSTe unit cell without and with SOC. As can be observed from the panel (a) of the figure, as expected, all the bands are spin degenerate in the absence of SOC. However, when the SOC is included, we observe a Rashba spin splitting around the Γ and M points of the VBM and CBM, respectively. This is also confirmed from the spin texture plotted in $k_x - k_y$ plane around the Γ point of the VBM (Fig. 4). As can be observed from the figure, near the zone center, the in-plane spin-polarized states dominate the texture, with almost no perpendicular component of the spin. It should however be noted that the splitting around the M point of CBM is very small compared to that of around Γ point in VBM. So, for further analysis and to quantify the effect we consider the splitting around Γ point. The Rashba parameter could be obtained using the energy difference (E_R) and the momentum offset (k_R) using the relation $\alpha_R = 2E_R/k_R$ along both $\Gamma - K$ and $\Gamma - M$ directions (Figs. 3(b) and 3(e)). The values of α_R are obtained as 422 and 356 meVÅ along $\Gamma - K$ and $\Gamma - M$ directions, respectively. These are in good agreement with the literature values of 322 and 324, respectively for WSTe [42].

TABLE I. Calculated lattice parameters, Wyckoff positions, binding energies, band gaps, spin polarization, and bond lengths and bond angles for TM-WSTe structures.

	Lattice constants (Å)	L ₁ (Å)	L ₂ (Å)	θ (degrees)	
WSTe	3.31 [Present work] 3.35 [37] 3.36 [38]	2.429	2.718	83.11	
Fe-WSTe	3.31 [Present work]	2.282	2.623	82.44	
Co-WSTe	3.31 [Present work]	2.261	2.619	81.63	
Mn-WSTe	3.31 [Present work]	2.319	2.626	83.06	
Wyckoff positions		<i>x</i>	<i>y</i>	<i>z</i>	
	W	0.6667	0.3333	0.7550	
	S	0.3333	0.6667	0.8067	
	Te	0.3333	0.6667	0.6883	
% con.	Space group	Binding ene. (eV)	Bandgap (eV)	Phase	Spin-pol. (%)
Fe-WSTe					
6.25	156	-37.220	0.000 (↑), 1.150 (↓)	Half-met.	100
12.50	8	-40.984	0.051 (↑), 0.536 (↓)	Semic.	-
18.75	156	-45.602	0.000 (↑), 0.949 (↓)	Half-met.	100
25	156	-49.433	0.113 (↑), 1.079 (↓)	Semic.	-
Mn-WSTe					
6.25	156	-39.329	0.102 (↑), 1.208 (↓)	Semic.	-
12.50	8	-44.249	0.024 (↑), 0.593 (↓)	Semic.	-
18.75	156	-50.938	0.024 (↑), 1.140 (↓)	Semic.	-
25	156	-56.315	0.000 (↑), 1.161 (↓)	Half-met.	100
Co-WSTe					
6.25	156	-37.660	0.077 (↑), 0.602 (↓)	Semic.	-
12.50	8	-39.782	0.051 (↑), 0.067 (↓)	Semic.	-
18.75	156	-42.981	0.000 (↑), 0.597 (↓)	Half-met.	100
25	156	-45.700	0.000 (↑), 0.332 (↓)	Half-met.	100

Our computed values of α_R are also consistent with the reported values for other TMDs such as MoSeTe and WSeTe [42]. It should be noted that a large Rashba spin splitting is preferable for spintronics based device applications. For Zeeman splitting, we observed a large spin splitting of 403 meV at K and K' valleys of the valence band (Fig. 3(d)). Compared to the valence band, the conduction band edges show a minor spin splitting of ~ 37 meV. Our calculated values are in good agreement with the reported values, 426 and 29 meV, respectively, in the case of WSTe [43].

One of the efficient mechanisms to tune the magnitude of Rashba spin splitting in TMDs is reported through the application of strain [42]. The other proposed mechanisms could be the external electric field and charge dopings [44–46]. Considering this, as the strain is reported to have more impact [47, 48], next we examine the effects of uniaxial and biaxial strains on Rashba and Zeeman-spin splittings. For this, we apply an uniaxial (x -direction) and biaxial compressive and tensile strains of up to 3%. The strained evolved band gap, Rashba parameter and Zeeman spin splitting energy from our simulations are shown in Fig. 5. As discernible from the panel (a) of the figure, band gap is observed to increase slowly with compressive strain, whereas the application of tensile strains reduces it, with biaxial strain showing more profound impact at larger strains. The observed trend is consistent with the

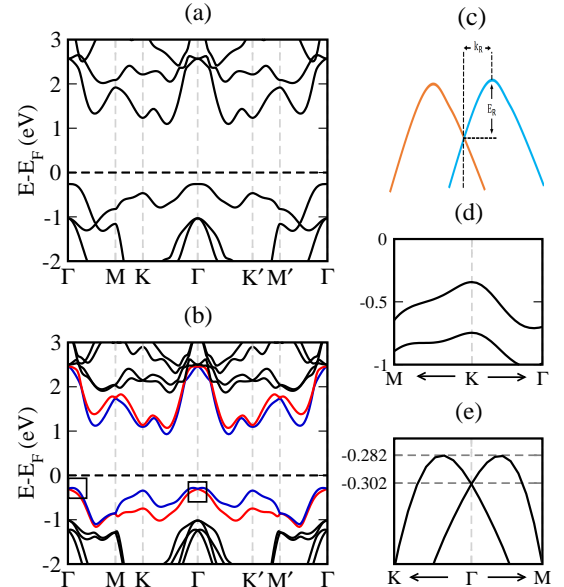


FIG. 3. The electronic band structure of WSTe unit cell, (a) without and (b) with spin-orbit coupling. (c) A schematic diagram showing Rashba spin splitting. (d) The zoomed view of Rashba splitting at the Γ point of VBM. (e) The zoomed view of Zeeman splitting at K -point of VBM.

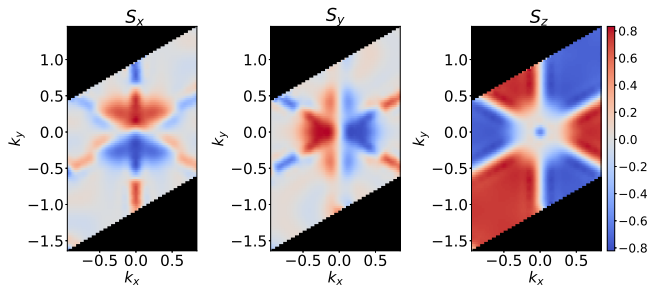


FIG. 4. The spin texture of VBM around Γ point in $k_x - k_y$ plane at 0.29 eV. Red and blue colors represent the spin up and spin down states, respectively.

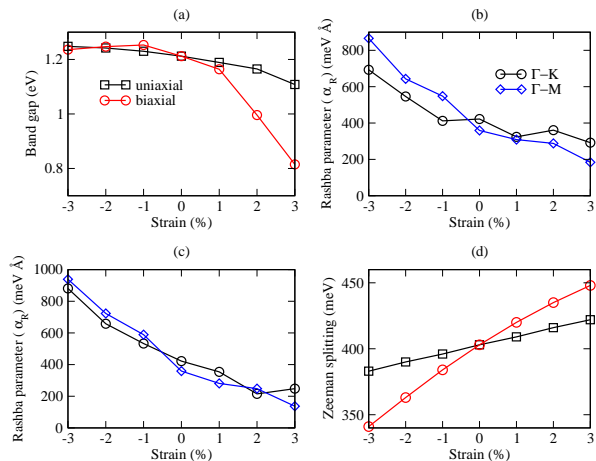


FIG. 5. (a) The strain evolution of band gap. (b), (c) Rashba parameter under uniaxial and biaxial strains, respectively. (d) Zeeman spin splitting in WSTe.

findings in the literature [49]. The computed α_R along both $\Gamma - K$ and $\Gamma - M$ directions are observed to show an overall increasing (decreasing) trend with compressive (tensile) uniaxial and biaxial strains (panels (b) and (c)). It is consistent with reported literature [42]. We find an enhancement of about 1.64% and 2.43% in α_R for $\Gamma - K$ and $\Gamma - M$ directions, respectively for 3% of compressive uniaxial strain. In the case of 3% compressive biaxial strain, an enhancement is about 2.08% and 2.63% for $\Gamma - K$ and $\Gamma - M$ directions, respectively. Interestingly, the Zeeman splitting show an opposite trend of evolution than Rashba splitting. We observe an almost a linear decrease (increase) in the splitting energy as a function of compressive (tensile) strains.

Next, we examine the electronic structure of TM-substituted WSTe. Fig. 6 shows the spin-polarized electronic band structure of Fe-WSTe for 6.25%, 12.5%, 18.75%, and 25% concentrations. The upper panels show the data for spin-up channel, whereas the lower panels represent the spin down channel. As discernible from the figure, for 6.25 and 18.75% concentration of Fe, we observe a metallic behavior in the spin-up channel, whereas the spin-down channel exhibits a semiconducting behavior with band gaps of 1.15 and 0.95 eV for 6.25% and 18.75%, respectively. This mixed nature

of electronic structure suggests the half-metallic character of Fe-WSTe. Such materials could be crucial for promoting the spin-polarized transport in spintronics applications [50]. On contrary, in the case of 12.5 and 25% concentrations, both the spin-up and down channels show a semiconducting nature; however, with a difference in the band gaps for spin-up and down channels. As evident from the Table I, for 12.5%, the spin-up channel has a small band gap opening of ~ 0.05 eV, whereas the spin down channel has an order more band gap of ~ 0.54 eV. Similarly, for the case of 25% concentration, spin-up and down band gaps are ~ 0.11 and ~ 1.10 , respectively. So, based on our predicted nature of electronic structure, one can conclude that the intrinsic properties of pristine WSTe could be tailored to exhibit either half-metallic or semiconducting characteristics depending on the need for device applications. The band gap modulation observed is significant for developing advanced spintronics devices which require a precise control over the spin-polarized transport [3].

To get insight into the origin of half-metallicity in Fe-WSTe, next we examined the atom-projected density of states (pDOS) for Fe-WSTe. The data from our calculations are shown in Fig. 7 for all the concentrations. Comparing with pristine WSTe, we observed that the $5d$ -electrons of W remain the dominant contributing states in both the valence and conduction bands for all the concentrations. Like W, Fe is also observed to contribute to both valence and conduction bands, however, with smaller magnitudes and more dominantly for the spin down channel. Consistent with the band structure, for 6.25 and 18.72% of Fe, for the majority spin, we observe non zero states at the Fermi level. As discernible from the insets of the figure, these contributions arise from the $3d$ and $5d$ -electrons of Fe and W atoms, respectively. The absence of states at Fermi level for spin down channel leads to a 100% spin polarization for these concentrations. For the case of 18.75 and 25% concentrations, however, while spin down channel exhibits no states at Fermi level, there is a small band gap opening in the majority spin. Our obtained electronic structure of Fe-WSTe is consistent with the reported data for another material of Janus family, Fe-MoSeTe [39]

C. Magnetic properties

Next, we present and analyze our data on magnetic properties of TM-WSTe. The TM substitutions in non-magnetic 2D materials are observed to introduce magnetic degree of freedom in the materials [5, 51]. First we investigate the ground state magnetic configuration of TM-WSTe systems. For this, we examined both ferromagnetic (FM) and antiferromagnetic (AFM) orientations of magnetic moments for all the Fe/Mn/Co concentrations. In Table II, we have provided the relative energy for FM phase with respect to AFM. As evident from the table, our calculations reveal the actual ground state of Fe-WSTe as a FM phase for all the concentrations. The FM energy is found to be $\approx 0.55, 0.28, 0.12,$ and 0.37 eV lower than that of AFM phase for 6.25, 12.5, 18.75, and 25% concentrations, respectively. We observe a similar trend for Mn-WSTe and Co-WSTe systems, where FM configuration is

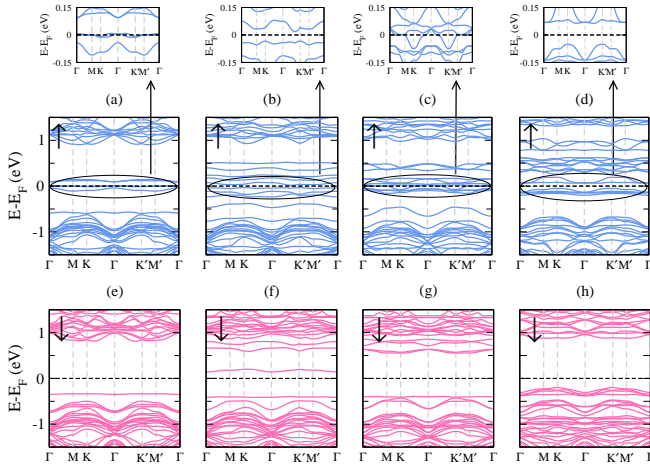


FIG. 6. The spin polarized band structure for Fe-WSTe without SOC, (a) 6.25%, (b) 12.5%, (c) 18.75%, and (d) 25% Fe-substitution, respectively. The upper panels show the spin-up contribution, whereas the down panels show the spin-down states. The Fermi level is at zero. The zoomed view near Fermi level has also been shown.

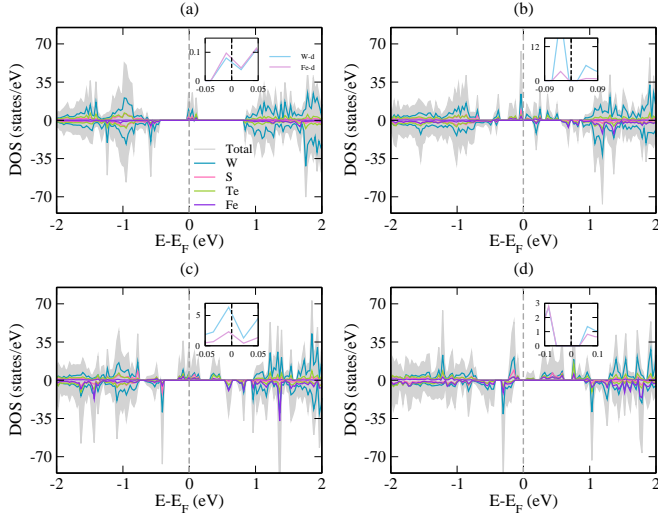


FIG. 7. The spin-polarized total and atom-projected density of states for Fe-WSTe, (a) 6.25%, (b) 12.5%, (c) 18.75%, and (d) 25%, respectively. The Fermi level is at zero.

observed to be the actual ground state magnetic configuration, except for 25% Co-WSTe.

Examining the total magnetic moments provided in Table II, as can be expected, our simulations predict a zero magnetic moment for pristine WSTe, which is in agreement with the literature data [52, 53]. However, for TM-WSTe, we observe nonzero magnetic moments with a trend of increasing magnitudes, except for 25% in the case of Fe and Co, with concentrations (panel (a) of Fig. 8). The reason for the increase in total magnetic moment could be attributed to the increasing ferromagnetic exchange between neighboring Fe/Mn/Co ions at higher concentrations. The decrease in the value of total magnetic moment in Fe and Co for 25% concentration could be attributed to the reduction in the magnetic moments

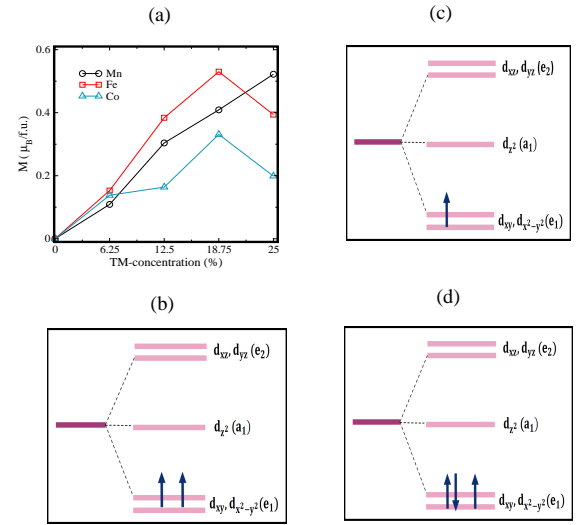


FIG. 8. (a) Magnetic moment as a function of Fe, Mn and Co concentration in TM-WSTe. Octahedral filling of d -electrons in Fe-WSTe (panel (b)), Mn-WSTe (panel (c)), and Co-WSTe (panel (d)) systems.

of Fe and Co atoms due to an increased hybridization between Fe/Co- $3d$ and WSTe states (specially p -electrons of S and Te atoms). Also, at this concentration, W, S, and Te atoms have more opposite contributions, which reduces the total magnetic moment.

For Mn-WSTe, the largest total magnetic moment is obtained as $0.522 \mu_B/\text{f.u.}$ for the highest concentration of 25%. Similarly, for Fe-WSTe and Co-WSTe, these are 0.530 and $0.331 \mu_B/\text{f.u.}$, respectively, for 18.75% concentration. Our obtained magnetic moments for Fe/Mn/Co-WSTe for 6.25% are in good agreement with the previous study on parent compound TM-WS₂ [54]. As can be observed from the table, the dominant contribution to total magnetic moment comes from the TM-elements. For example, for 6.25%, we observe ≈ 133 , 189 , and 66% of contributions to total magnetic moment from Fe, Mn, and Co, respectively. The reason for this dominant contribution could be ascribed to the presence of unpaired d -electrons in these elements. This is shown in the octahedral filling of $3d$ -electrons in Fe/Mn/Co-WSTe in Fig. 8. Interestingly, there are significant contributions of opposite phase from W, S and Te atoms through the interaction with TM-elements. The opposite sign leads to cancellations, and hence reduces the total magnetic moment.

To get further insight into the spin orientation and resultant nonzero magnetic moments in TM-WSTe, next we examined the spin density distribution in these systems. Fig. 9 shows the Isosurface plots for the spin charge density of Fe-WSTe for pristine WSTe, and 6.25 and 25% concentrations. The spin charge density is defined as $\Delta\rho = \rho_{\uparrow} - \rho_{\downarrow}$, where ρ_{\uparrow} and ρ_{\downarrow} represent the spin-up and spin-down charge densities [23]. As can be expected, for pristine WSTe, the spin density distribution is uniform across the plane of the material (panel (a)), and as a result it leads to the zero spin polarization. For Fe-WSTe, however, the spin density distribution is observed to be more localized with Fe atoms. This suggests a charge transfer

TABLE II. The relative energy ($\Delta E = E_{\text{FM}} - E_{\text{AFM}}$) (in eV) of FM and AFM configurations and the atom resolved magnetic moments (in μ_B/atom) for TM-substituted WSTe for all considered concentrations.

% con.	ΔE	μ^{W}	μ^{S}	μ^{Te}	$\mu^{\text{Fe/Mn/Co}}$	μ^{Tot}
WSTe		0.0	0.0	0.0	0.0	0.0
Fe-WSTe						
6.25	-0.559	-0.047	-0.000	-0.007	3.276	2.451
12.5	-0.285	-0.014	-0.003	-0.000	3.202	6.139
18.75	-0.129	-0.041	-0.014	-0.007	3.127	8.482
25	-0.376	-0.150	-0.061	-0.079	2.590	6.310
Mn-WSTe						
6.25	-1.063	-0.050	-0.021	-0.028	3.308	1.749
12.5	-0.244	-0.058	-0.035	-0.040	3.445	4.864
18.75	-0.192	-0.136	-0.058	-0.063	3.429	6.559
25	-0.264	-0.174	-0.077	-0.094	3.392	8.358
Co-WSTe						
6.25	-0.125	0.063	-0.014	0.002	1.454	2.212
12.5	-0.092	-0.014	-0.025	-0.013	1.732	2.636
18.75	-0.026	-0.028	-0.008	0.001	1.925	5.296
25	+0.017	-0.051	-0.066	-0.035	1.358	3.187

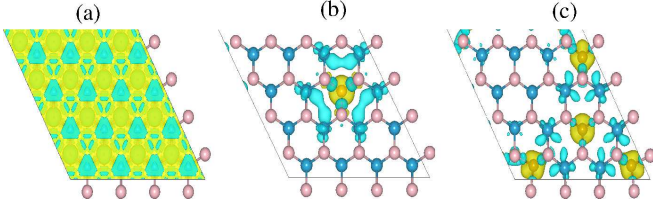


FIG. 9. Isosurface plots for the spin charge density, (a) pristine WSTe (b) 6.25%, and (d) 25% Fe-WSTe monolayer. The Isosurface value is extracted to be $0.003 e/\text{\AA}^3$.

between TM elements and WSTe, leading to a nonzero spin polarization in the system.

D. Valley Polarization

Next, we present and discuss our simulation results on the valley polarization. Valley polarization in 2D materials is induced as a combined effect of broken time reversal symmetry, which could be introduced via TMs dopings, and a strong spin-orbit coupling [23]. The schematic representation of valley polarization is shown in panel (a) of Fig. 10. The valley polarization can be quantified in terms of the energy difference, $\Delta_{KK'} = |E_{K'} - E_K|$, between the K and K' valleys. Panels (b, c, d, e) of Fig. 10 shows the electronic band structure of Fe-WSTe in the presence of SOC for all the chosen concentrations. We have two key observations from the figure. First, the defect states emerge in the vicinity of the Fermi level. These defect states mainly comprise of W and Fe atoms, which suggests a strong orbital hybridization between these atoms. And second, the spin degeneracy in the bands is lifted. Because of the opposite spins associated with K and K' valleys due to broken time-reversal symmetry, there is an uneven splitting of the energy levels at these valleys of VBM

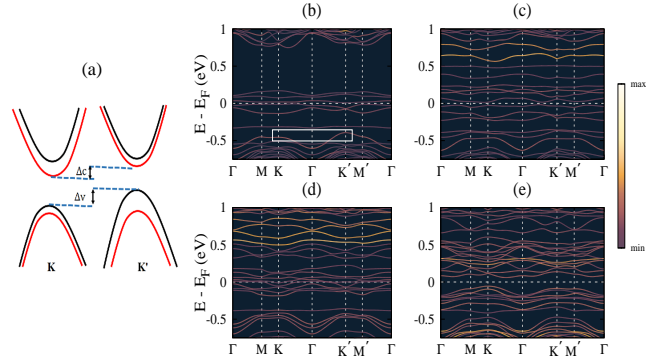


FIG. 10. (a) A schematic diagram representing the valley polarization in TM-WSTe. The spin-orbit coupled band structures of Fe-WSTe for 6.25 (panel (b)), 12.5 (panel (c)), 18.75 (panel (d)), and 25% (panel (e)) concentrations. The rectangular box is to indicate the band used in the calculation of valley polarization.

and CBM. As can be observed from panel (b), for 6.25% Fe-WSTe, the spin splitting at CBM is much smaller than that at the VBM. The reason for this could be attributed to the different orbital's contribution to the edges of VBM and CBM – d_{z^2} is observed to have dominant contribution to CBM, whereas the VBM is populated mainly by d_{xy} and $d_{x^2-y^2}$ orbitals. As can be observed from panel (b), for 6.25% concentration, the spin splitting at K valley is larger than that at K' , leading to a valley polarization of ~ 65 meV. This observed value of valley polarization from our calculations for Fe-WSTe is significantly higher than the previously reported values, 58 meV, for transition metal (V) doped-WSSe [23]. For higher concentrations (panels (c), (d), and (e)), we observe an increase population of defect states in the vicinity of Fermi level and within the band gap. This leads the deformation of valleys and makes it difficult to distinguish between the defects and valley-polarized states. So, as a result, it is extremely challenging to accurately quantify the valley polarization for these concentrations.

Since the valley polarization is a key parameter and governs various phenomena like anomalous valley Hall effects, valley transport, valley-polarized superconductivity and valley-based quantum computing [15, 55], it is crucial to explore the mechanisms to enhance it. One of the most common and feasible approach to enhance valley polarization effects in 2D materials is through the application of strain [56, 57]. Considering this, next we examine the effects of uniaxial and biaxial strains on valley polarization properties of TM-WSTe. Fig. 11 shows the electronic band structure for 6.25% Fe-WSTe at different compressive and tensile uniaxial strains. As can be observed from the figures, the energy difference between the K and K' valleys at the VBM increases (decreases) with increasing tensile (compressive) strain. This leads to an increase (decrease) in the valley polarization values as function of tensile (compressive) strain (Fig. 13(a)). The maximum valley polarization is obtained as 78 meV for 3% of tensile strain. We observe a similar trend for $\Delta E_{KK'}$ as the function of biaxial strain also (Fig. 13(a)), however, with a key difference. The change in the valley polarization with strain is

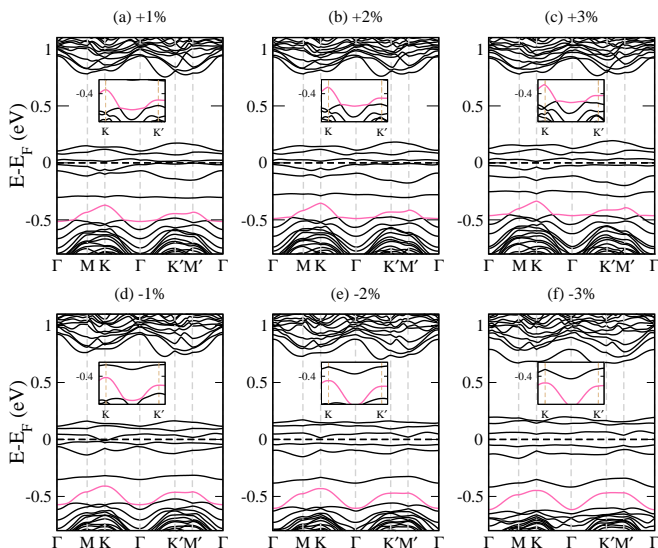


FIG. 11. Electronic band structure of 6.25% Fe-WSTe under the uniaxial strain, (a) +1% (b) +2% (c) +3% (d) -1% (e) -2% and (f) -3%. The Fermi level is at 0 eV.

more profound in the case of biaxial strain. We could achieve a maximum valley polarization of 112 meV with an application of 3% biaxial tensile strain. These findings suggest that with the help of moderate strain engineering one can tune the valley polarization of TM-WSTe. Our results further highlight that Fe-WSTe could be a promising candidate for valleytronic applications. In contrast to traditional charge-based electronics, valleytronics offer a low-energy information processing, as the transition between valley states requires minimal energy [10, 58, 59]. Real-time control of valley polarization can be used in high-speed transistors, non-volatile memory devices, and innovative quantum computing applications [60–62].

TABLE III. Valley polarization at different uniaxial and biaxial strains for 6.25% Fe-WSTe.

Uniaxial Strain (%)	$\Delta_{KK'}$ (meV)	Biaxial Strain (%)	$\Delta_{KK'}$ (meV)
-3	22	-3	8
-2	40	-2	35
-1	54	-1	46
0	65	0	65
+1	73	+1	84
+2	77	+2	102
+3	78	+3	112

IV. CONCLUSIONS

In summary, with the help of density functional theory based first-principles calculations, we have examined the effect of transition metal substitution on the electronic, magnetic, and valleytronic properties of WSTe monolayer. In agreement with the literature data [42], our simulations on electronic structure predict WSTe as an indirect bandgap

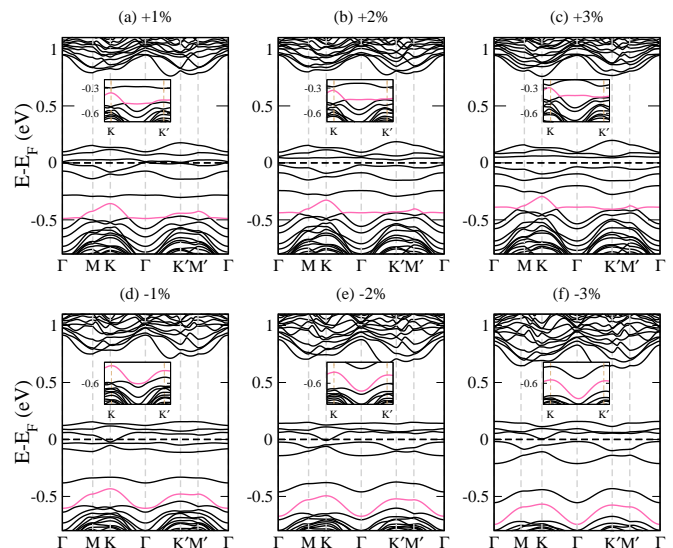


FIG. 12. Electronic band structure of 6.25% Fe-WSTe under the biaxial strain, (a) +1% (b) +2% (c) +3% (d) -1% (e) -2% and (f) -3%. The Fermi level is at 0 eV.

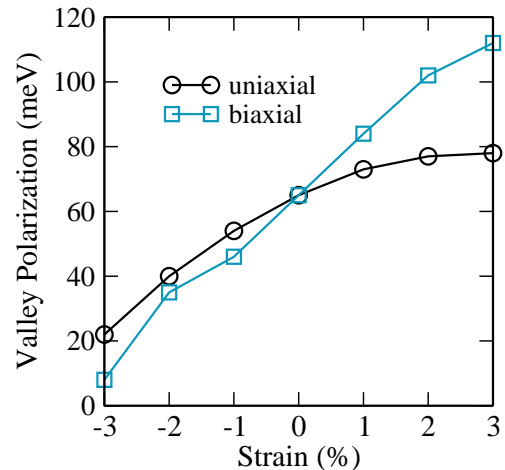


FIG. 13. Valley polarization as a function of uniaxial and biaxial strain for 6.25% concentration in Fe-WSTe.

semiconductor. Our computed bandgap, 1.35 eV, agrees well with previous data [42]. The WSTe monolayer is found to inherently exhibit Rashba and Zeeman-spin splittings due to the intrinsic out-of-plane electric field and in-plane inversion symmetry breaking, respectively, along with a strong spin-orbit coupling. Our obtained Rashba parameter and Zeeman-spin splitting are 422 meVÅ and 403 meV, respectively. Our strain dependent calculations show an increasing(decreasing) trend of Rashba parameter with compressive(tensile) uniaxial and biaxial strains. Interestingly, the Zeeman splitting is observed to show a linear dependence on strain with an opposite trend of decreasing(increasing) energy with compressive(tensile) strains.

From the electronic structure of TM-WSTe, we observed an emergence of half-metallic ferromagnetism with 100% spin polarization for 6.25 and 18.75% of Fe, 25% of Mn, and 18.75

and 25% of Co structures. The largest effective magnetic moments for supercell are obtained as 8.5, 8.4 and 5.3 μ_B for Fe/Mn/Co-WSTe structures, respectively. Our simulations on valley polarization predict the values 65, 54.4 and 46.3 meV for 6.25% of Fe, Mn and Co substitution, respectively. Our calculations show a strain dependent tunability of valley polarization, where it is observed to increase(decrease) with tensile(compressive) uniaxial and biaxial strains. For Fe-WSTe, a maximum valley polarization of 112 is obtained with an application 3% biaxial strain. The observed significant values of spin-polarization, Rashba splitting and valley polarization suggest that TM-WSTe could offer a potential candidate for

spintronics and valleytronics applications.

ACKNOWLEDGMENTS

BKM acknowledges the funding support from SERB, DST (CRG/2022/000178). Shivani acknowledges the fellowship support from UGC (BININ01949131), Govt. of India. The calculations are performed using the High Performance Computing cluster Tejas at the Indian Institute of Technology Delhi and PARAM Rudra, IUAC, New Delhi.

-
- [1] E. C. Ahn, 2d materials for spintronic devices, *npj 2D Materials and Applications* **4**, 17 (2020).
- [2] A. Avsar, H. Ochoa, F. Guinea, B. Özyilmaz, B. Van Wees, and I. J. Vera-Marun, Colloquium: Spintronics in graphene and other two-dimensional materials, *Reviews of Modern Physics* **92**, 021003 (2020).
- [3] Y. Liu, C. Zeng, J. Zhong, J. Ding, Z. M. Wang, and Z. Liu, Spintronics in two-dimensional materials, *Nano-Micro Letters* **12**, 1 (2020).
- [4] L. Jin, X. Zhang, Y. Liu, X. Dai, and G. Liu, Theoretical realization of two-dimensional half-metallicity and fully spin-polarized multiple nodal-line fermions in monolayer probr, *Phys. Rev. B* **105**, 075414 (2022).
- [5] S. Fu, K. Kang, K. Shayan, A. Yoshimura, S. Dadras, X. Wang, L. Zhang, S. Chen, N. Liu, A. Jindal, *et al.*, Enabling room temperature ferromagnetism in monolayer mos₂ via in situ iron-doping, *Nature communications* **11**, 2034 (2020).
- [6] S. J. Yun, D. L. Duong, D. M. Ha, K. Singh, T. L. Phan, W. Choi, Y.-M. Kim, and Y. H. Lee, Ferromagnetic order at room temperature in monolayer wse₂ semiconductor via vanadium dopant, *Advanced Science* **7**, 1903076 (2020).
- [7] P. M. Coelho, H.-P. Komsa, K. Lasek, V. Kalappattil, J. Karthikeyan, M.-H. Phan, A. V. Krashennikov, and M. Batzill, Room-temperature ferromagnetism in mote₂ by post-growth incorporation of vanadium impurities, *Advanced Electronic Materials* **5**, 1900044 (2019).
- [8] Z. Muhammad, H. Lv, C. Wu, M. Habib, Z. ur Rehman, R. Khan, S. Chen, X. Wu, and L. Song, Room temperature ferromagnetism in fe-doped semiconductor zrs₂ single crystals, *Materials Research Express* **5**, 046110 (2018).
- [9] X. Jiang, X. Zhang, F. Xiong, Z. Hua, Z. Wang, and S. Yang, Room temperature ferromagnetism in transition metal-doped black phosphorous, *Applied Physics Letters* **112**, 10.1063/1.5022540 (2018).
- [10] C. Luo, Z. Huang, H. Qiao, X. Qi, and X. Peng, Valleytronics in two-dimensional magnetic materials, *Journal of Physics: Materials* **7**, 022006 (2024).
- [11] D. Xiao, W. Yao, and Q. Niu, Valley-contrasting physics in graphene: Magnetic moment and topological transport, *Phys. Rev. Lett.* **99**, 236809 (2007).
- [12] H. Zeng, J. Dai, W. Yao, D. Xiao, and X. Cui, Valley polarization in mos₂ monolayers by optical pumping, *Nature nanotechnology* **7**, 490 (2012).
- [13] J. Qi, X. Li, Q. Niu, and J. Feng, Giant and tunable valley degeneracy splitting in mote₂, *Phys. Rev. B* **92**, 121403 (2015).
- [14] A. Soni and S. K. Pal, Valley degree of freedom in two-dimensional van der waals materials, *Journal of Physics D: Applied Physics* **55**, 303003 (2022).
- [15] S. A. Vitale, D. Nezich, J. O. Varghese, P. Kim, N. Gedik, P. Jarillo-Herrero, D. Xiao, and M. Rothschild, Valleytronics: opportunities, challenges, and paths forward, *Small* **14**, 1801483 (2018).
- [16] A. B. Khanikaev, N. Arju, Z. Fan, D. Purtseladze, F. Lu, J. Lee, P. Sarriguarte, M. Schnell, R. Hillenbrand, M. Belkin, *et al.*, Experimental demonstration of the microscopic origin of circular dichroism in two-dimensional metamaterials, *Nature communications* **7**, 1 (2016).
- [17] K. F. Mak, K. L. McGill, J. Park, and P. L. McEuen, The valley hall effect in mos₂ transistors, *Science* **344**, 1489 (2014).
- [18] Y. Saito, Y. Nakamura, M. S. Bahramy, Y. Kohama, J. Ye, Y. Kasahara, Y. Nakagawa, M. Onga, M. Tokunaga, T. Nojima, *et al.*, Superconductivity protected by spin-valley locking in ion-gated mos₂, *Nature Physics* **12**, 144 (2016).
- [19] Y. Cheng, Q. Zhang, and U. Schwingenschlögl, Valley polarization in magnetically doped single-layer transition-metal dichalcogenides, *Physical Review B* **89**, 155429 (2014).
- [20] K. F. Mak, K. He, J. Shan, and T. F. Heinz, Control of valley polarization in monolayer mos₂ by optical helicity, *Nature nanotechnology* **7**, 494 (2012).
- [21] K. R. Sahoo, J. J. Panda, S. Bawari, R. Sharma, D. Maity, A. Lal, R. Arenal, G. Rajalaksmi, and T. N. Narayanan, Enhanced room-temperature spin-valley coupling in v-doped mos₂, *Phys. Rev. Mater.* **6**, 085202 (2022).
- [22] R. Peng, Y. Ma, S. Zhang, B. Huang, and Y. Dai, Valley polarization in janus single-layer mos₂ via magnetic doping, *The Journal of Physical Chemistry Letters* **9**, 3612 (2018).
- [23] X. Zhao, B. Qiu, G. Hu, W. Yue, J. Ren, and X. Yuan, Transition-metal doping/adsorption induced valley polarization in janus wse₂: First-principles calculations, *Applied Surface Science* **490**, 172 (2019).
- [24] X. Zhao, Y. Li, R. Liang, G. Hu, X. Yuan, and J. Ren, Enhanced valley polarization at valence/conduction band in transition-metal-doped wte₂ under strain force, *Applied Surface Science* **504**, 144367 (2020).
- [25] M.-H. Lv, C.-M. Li, and W.-F. Sun, Spin-orbit coupling and spin-polarized electronic structures of janus vanadium-dichalcogenide monolayers: First-principles calculations, *Nanomaterials* **12**, 382 (2022).
- [26] Y. Wang, W. Wei, H. Wang, N. Mao, F. Li, B. Huang, and Y. Dai, Janus tixy monolayers with tunable berry curvature,

The journal of physical chemistry letters **10**, 7426 (2019).

- [27] W. Liu, X. Li, C. Zhang, and S. Yan, Janus vxy monolayers with tunable large berry curvature, *Journal of Semiconductors* **43**, 042501 (2022).
- [28] G. Kresse and D. Joubert, From ultrasoft pseudopotentials to the projector augmented-wave method, *Phys. Rev. B* **59**, 1758 (1999).
- [29] G. Kresse and J. Hafner, Ab initio molecular-dynamics simulation of the liquid-metal–amorphous-semiconductor transition in germanium, *Phys. Rev. B* **49**, 14251 (1994).
- [30] G. Kresse and J. Furthmüller, Efficient iterative schemes for ab initio total-energy calculations using a plane-wave basis set, *Phys. Rev. B* **54**, 11169 (1996).
- [31] J. P. Perdew, K. Burke, and M. Ernzerhof, Generalized gradient approximation made simple, *Phys. Rev. Lett.* **77**, 3865 (1996).
- [32] P. E. Blöchl, Projector augmented-wave method, *Phys. Rev. B* **50**, 17953 (1994).
- [33] S. L. Dudarev, G. A. Botton, S. Y. Savrasov, C. J. Humphreys, and A. P. Sutton, Electron-energy-loss spectra and the structural stability of nickel oxide: An lsd+u study, *Phys. Rev. B* **57**, 1505 (1998).
- [34] M. Cococcioni and S. de Gironcoli, Linear response approach to the calculation of the effective interaction parameters in the LDA + U method, *Phys. Rev. B* **71**, 035105 (2005).
- [35] C. E. Calderon, J. J. Plata, C. Toher, C. Oses, O. Levy, M. Fornari, A. Natan, M. J. Mehl, G. Hart, M. B. Nardelli, *et al.*, The afflow standard for high-throughput materials science calculations, *Computational Materials Science* **108**, 233 (2015).
- [36] G. Lucovsky, R. M. White, J. A. Benda, and J. F. Revelli, Infrared-reflectance spectra of layered group-iv and group-vi transition-metal dichalcogenides, *Phys. Rev. B* **7**, 3859 (1973).
- [37] D. Er, H. Ye, N. C. Frey, H. Kumar, J. Lou, and V. B. Shenoy, Prediction of enhanced catalytic activity for hydrogen evolution reaction in janus transition metal dichalcogenides, *Nano Letters* **18**, 3943 (2018), pMID: 29756785.
- [38] C. Xia, W. Xiong, J. Du, T. Wang, Y. Peng, and J. Li, Universality of electronic characteristics and photocatalyst applications in the two-dimensional janus transition metal dichalcogenides, *Phys. Rev. B* **98**, 165424 (2018).
- [39] Y. Li, B. Qiu, X. Zhao, G. Hu, W. Yue, X. Yuan, and J. Ren, Spin polarization properties of two-dimensional mosete induced by transition-metal doping: first-principles calculations, *The European Physical Journal B* **92**, 1 (2019).
- [40] R. Ahammed and A. De Sarkar, Valley spin polarization in two-dimensional $h-mN$ ($m = Nb, ta$) monolayers: Merger of valleytronics with spintronics, *Phys. Rev. B* **105**, 045426 (2022).
- [41] Y. A. Bychkov and E. Rashba, Properties of a 2d electron gas with lifted spectral degeneracy, *pis' ma zh, Eksp. Teor. Fiz* **39**, 66 (1984).
- [42] T. Hu, F. Jia, G. Zhao, J. Wu, A. Stroppa, and W. Ren, Intrinsic and anisotropic rashba spin splitting in janus transition-metal dichalcogenide monolayers, *Phys. Rev. B* **97**, 235404 (2018).
- [43] Y. Cheng, Z. Zhu, M. Tahir, and U. Schwingenschlögl, Spin-orbit-induced spin splittings in polar transition metal dichalcogenide monolayers, *Europhysics Letters* **102**, 57001 (2013).
- [44] S.-J. Gong, C.-G. Duan, Y. Zhu, Z.-Q. Zhu, and J.-H. Chu, Controlling rashba spin splitting in au(111) surface states through electric field, *Phys. Rev. B* **87**, 035403 (2013).
- [45] K. V. Shanavas and S. Satpathy, Electric field tuning of the rashba effect in the polar perovskite structures, *Phys. Rev. Lett.* **112**, 086802 (2014).
- [46] J. Chen, K. Wu, H. Ma, W. Hu, and J. Yang, Tunable rashba spin splitting in janus transition-metal dichalcogenide monolayers via charge doping, *RSC Adv.* **10**, 6388 (2020).
- [47] S. Postorino, D. Grassano, M. D'Alessandro, A. Pianetti, O. Pulci, and M. Palummo, Strain-induced effects on the electronic properties of 2d materials, *Nanomaterials and Nanotechnology* **10**, 1847980420902569 (2020).
- [48] Y. Sun and K. Liu, Strain engineering in functional 2-dimensional materials, *Journal of Applied Physics* **125**, 10.1063/1.5053795 (2019).
- [49] J. El Hamdaoui, L. M. Pérez, M. Ojeda-Martínez, N. El Ouarie, P. Díaz, D. Laroze, and E. M. Feddi, First principle study on the effect of strain on the electronic structure and carrier mobility of the janus moste and wste monolayers, *Nanomaterials* **13**, 2535 (2023).
- [50] I. Choudhuri, P. Bhauriyal, and B. Pathak, Recent advances in graphene-like 2d materials for spintronics applications, *Chemistry of Materials* **31**, 8260 (2019).
- [51] G. Anagha, A. K. Jena, and J. Mohanty, Effect of nm (b, c, n, o and f) doping and femm co-doping on structure, electronic and magnetic properties of monolayer 2hmote2: A first principle investigation, *Physica E: Low-dimensional Systems and Nanostructures* **156**, 115846 (2024).
- [52] M. A. U. Absor, H. Kotaka, F. Ishii, and M. Saito, Tunable spin splitting and spin lifetime in polar wste monolayer, *Japanese Journal of Applied Physics* **57**, 04FP01 (2018).
- [53] X. Tang and L. Kou, 2d janus transition metal dichalcogenides: Properties and applications, *physica status solidi (b)* **259**, 2100562 (2022).
- [54] Y. Yang, X.-L. Fan, and H. Zhang, Effect of strain on the magnetic states of transition-metal atoms doped monolayer ws2, *Computational Materials Science* **117**, 354 (2016).
- [55] W.-Y. Tong, S.-J. Gong, X. Wan, and C.-G. Duan, Concepts of ferrovalley material and anomalous valley hall effect, *Nature communications* **7**, 13612 (2016).
- [56] C.-C. Hsu, M. Teague, J.-Q. Wang, and N.-C. Yeh, Nanoscale strain engineering of giant pseudo-magnetic fields, valley polarization, and topological channels in graphene, *Science Advances* **6**, eaat9488 (2020).
- [57] H. Zheng, B. Wu, S. Li, J. He, Z. Liu, C.-T. Wang, J.-T. Wang, J.-a. Duan, and Y. Liu, Strain-tunable valley polarization and localized excitons in monolayer wse 2, *Optics Letters* **48**, 2393 (2023).
- [58] V. Renard, B. Piot, X. Waintal, G. Fleury, D. Cooper, Y. Niida, D. Tregurtha, A. Fujiwara, Y. Hirayama, and K. Takashina, Valley polarization assisted spin polarization in two dimensions, *Nature communications* **6**, 7230 (2015).
- [59] K. Sakamoto, T.-H. Kim, T. Kuzumaki, B. Müller, Y. Yamamoto, M. Ohtaka, J. R. Osiecki, K. Miyamoto, Y. Takeichi, A. Harasawa, *et al.*, Valley spin polarization by using the extraordinary rashba effect on silicon, *Nature communications* **4**, 2073 (2013).
- [60] N. Rohling and G. Burkard, Universal quantum computing with spin and valley states, *New Journal of Physics* **14**, 083008 (2012).
- [61] A. Rycerz, J. Tworzydło, and C. Beenakker, Valley filter and valley valve in graphene, *Nature Physics* **3**, 172 (2007).
- [62] O. Gunawan, B. Habib, E. De Poortere, and M. Shayegan, Quantized conductance in an alas two-dimensional electron system quantum point contact, *Physical Review B—Condensed Matter and Materials Physics* **74**, 155436 (2006).